Predictive tools for the cooling rate-dependent microstructure evolution of AISI 316L stainless steel in additive manufacturing

Journal of Materials Research and Technology 29 (2024) 5530–5538

Contents lists available at ScienceDirect

Journal of Materials Research and Technology

journal homepage: www.elsevier.com/locate/jmrt

Predictive tools for the cooling rate-dependent microstructure evolution of AISI 316L stainless steel in additive manufacturing

Amirreza Abdali [a], Syamak Hossein Nedjad [a,**], Habib Hamed Zargari [a,***], Abdollah Saboori [b,*], Mehmet Yildiz [c,d,e]

[a] Faculty of Materials Engineering, Sahand University of Technology, P.O. Box: 51335-1996, Tabriz, Iran
[b] Integrated Additive Manufacturing Center, Department of Management and Production Engineering, Politecnico di Torino, Torino, Italy
[c] Faculty of Engineering and Natural Sciences, Sabanci University, Istanbul, Turkey
[d] Integrated Manufacturing Technologies Research and Application Center, Sabanci University, Istanbul, Turkey
[e] Composite Technologies Center of Excellence, Istanbul Technology Development Zone, Istanbul, Turkey

ARTICLE INFO

Handling Editor: L Murr

Keywords:
Stainless steel
Solidification
Mechanistic model
Constitution diagram
Additive manufacturing

ABSTRACT

This study presents a thorough evaluation of advanced predictive tools for the solidification microstructure of AISI 316L stainless steel, taking into account both chemical composition and cooling rate. In order to achieve a broad range of cooling rates comparable to prominent additive manufacturing processes, autogenous laser welds were carried out on the steel plate by means of powderless directed energy deposition (DED) and selective laser melting (SLM) machines. Computational analysis of cooling rates and metallographic investigations revealed that DED welds solidify at moderate rates, exhibiting a primary ferrite (FA) solidification mode. Conversely, SLM welds solidify at significantly higher rates, showing dual solidification modes: initial austenite (A) at the fusion boundary and subsequent ferrite (F) at the interior. The WRC-1992 constitution diagram predicts the FA mode in accordance with the findings in the DED welds. An implicated Schaeffler diagram, proposed for a comparable cooling rate, also predicts the same mode. An artificial neural network model, referred to as ORFN, consistently predicts the variation of ferrite content within the DED welds based on the cooling rate variation. The dual mode observed in the SLM welds aligns with established knowledge regarding the alteration of stainless steel solidification under extremely high cooling rates. While the occurrence of the A mode at the fusion boundary is anticipated according to implicated Schaeffler diagrams for extremely high cooling rates, the transition to the F mode is not addressed explicitly.

1. Introduction

Austenitic stainless steels are widely utilized in aerospace, chemical plants, oil and energy production, medical implants, and devices due to their exceptional corrosion resistance and mechanical properties [1]. Beyond traditional applications in the form of castings, wrought products, and weldments, these steels have found intensive use in additive manufacturing (3D printing) through processes such as directed energy deposition (DED), selective laser melting (SLM), wire arc additive manufacturing (WAAM), and fused filament fabrication (FFF) [2–7]. Solidification and subsequent cooling conditions govern the microstructure evolution of stainless steels during these processes thus significantly influencing the additively-manufactured parts as their performance is highly dependent on the microstructure. For example, residual ferrite strongly depends on the solidification and subsequent cooling conditions while it adversely impacts the corrosion resistance and thermal stability [8–10].

The solidification behavior of stainless steels is elucidated within the Fe–Cr–Ni ternary system and classified into four modes based on the primary phases crystallized from the melt: (i) mode A (single-phase austenite with no ferrite crystallized from the melt), (ii) mode AF (primary austenite with ferrite crystallized from the melt phase at the later stages of solidification), (iii) mode FA (primary ferrite with austenite crystallized from the melt phase at the later stages of solidification), and

* Corresponding author.
** Corresponding author.
*** Corresponding author.
E-mail addresses: hossein@sut.ac.ir (S. Hossein Nedjad), hhamedzargari@sut.ac.ir (H. Hamed Zargari), abdollah.saboori@polito.it (A. Saboori).

https://doi.org/10.1016/j.jmrt.2024.03.008
Received 14 January 2024; Received in revised form 1 March 2024; Accepted 1 March 2024
Available online 3 March 2024

(iv) mode F (single-phase ferrite with no austenite crystallized from the melt) [11,12]. The primary ferrite often undergoes phase transformation into austenite during cooling in the solid state. The extent and nature of this transformation significantly influences the microstructure at room temperature, resulting in diverse weld microstructures, e.g., austenite plus vermicular, skeletal, and lacy types residual ferrite, lathy austenite, Widmanstätten austenite, and massive austenite.

Significant efforts have been devoted to comprehending the microstructure of stainless steels within the welding context, in which predictive tools are extensively employed to discern weld metal microstructures and also appropriate compositions for base steels, weld consumables, and process conditions. The solidification mode of stainless steels can be predicted using the chromium equivalent (Cr_{eq}) and nickel equivalent (Ni_{eq}), solely based on the chemical composition [13]. The subsequent transformation of ferrite to austenite is also highly contingent on both the chemical composition and the initial solidification mode. Diverse methods have been utilized to predict the microstructure of stainless steel weld metals solely from their chemical composition. The primary aim has been to predict the amount of residual ferrite in the weld metals, expressed as the ferrite number, because a specific quantity of ferrite helps to prevent solidification cracking. The widely used tools for this purpose include the constitution diagrams of Schaeffler [14], DeLong [15], and WRC-1992 [16]. These diagrams have found extensive application in predicting the residual ferrite content in conventional weld metals [17,18]. Subsequently, models utilizing neural networks, solely relying on the chemical composition, have also been developed [19–21].

In addition to the chemical composition, the cooling rate significantly influences both the solidification mode and subsequent phase transformations. A high cooling rate, for instance, induces single-phase solidification modes (A and F), generates unusual eutectic and massive solidification modes, and modifies the amount of residual ferrite in both AF and FA modes [22,23]. These effects stem from the fact that a high cooling rate accelerates the solidification rate while decelerating the diffusional solid-state transformations. In the conventional welding range, the cooling rate effect may be negligible, and microstructure prediction relies primarily on alloy composition itself. However, in high-energy density welding and additive manufacturing, utilizing laser and electron beams, the cooling rate increases substantially which necessitates consideration of its effects. Vitek et al. [24], Brooks et al. [25], Katayama and Matsunawa [26], David et al. [27], Fukumoto et al. [28], Lippold [29], and Lienert [30] have extensively documented the impact of high cooling rates on the solidification behavior of stainless steel weld metals.

A high cooling rate practically implicates the constitution diagrams. For instance, Katayama and Matsunawa [26] determined implications to the Schaeffler diagram, based on pulsed laser welds. David et al. [27] reported implicated Schaeffler diagrams from pulsed laser welds of various commercial stainless steels. Nakao et al. [23] presented a series of implicated Schaeffler diagrams for stainless steel laser welds. A short review of implicated constitution diagrams is available in Ref. [31]. Advancing beyond the implicated constitution diagrams, an artificial neural network model, namely Oak Ridge Ferrite Number (ORFN), accounted for both chemical composition and cooling rate effects [32,33], providing more accurate predictions of the ferrite number compared to the WRC-1992 and the previous neural network model based solely on the chemical composition.

Several researchers have replicated the attributed welding metallurgy to predict the solidification microstructure of additively manufactured stainless steels [34–38]. However, due to significant cooling rate effects and a multitude of effective variables in additive manufacturing, there is a pressing need for a comprehensive prediction tool [39,40]. The integration of machine learning, mechanistic modeling, and metallurgy has been repeatedly emphasized for the development of such an efficient prediction tool in additive manufacturing [41–44]. Proceeding down this route, this paper incorporates mechanistic modeling and welding metallurgy to enhance the predictive capabilities of existing tools for determining the solidification microstructure of stainless steels in additive manufacturing. Given the widespread use of AISI 316L steel in various additive manufacturing processes and its high microstructure sensitivity to alloy composition even within the standard range [45–47], a plate of AISI 316L stainless steel with a composition closely aligned with the eutectic isopleth of the pseudo-binary Fe–Cr–Ni phase diagram was utilized in this study. The plate underwent autogenous welding using powderless DED and SLM machines, covering a broad range of cooling rates comparable to those encountered in additive manufacturing. Subsequently, experimental investigations, computational analyses of cooling rate, and available prediction tools were integrated to provide a comprehensive assessment of the solidification microstructure.

Table 1
A list of modeling variables.

Symbol	Nomenclature	Symbol	Nomenclature
P	Laser power	T	Temperature
η	Energy absorption coefficient	T_s, T_l	Solidus and liquidus temperatures
r	Laser beam radius	T_0	Ambient temperature
$\vec{v}$	Velocity vector	β	Thermal expansion coefficient
ρ	Density	γ_0	Surface tension of pure metal
p	Hydrodynamic pressure	U	Internal energy
μ	Kinematic viscosity	$\vec{n}$	Free surface normal
K	Drag coefficient	σ	Stefan-Boltzmann coefficient
f	Acceleration due to body force	ε	Radiation emissivity
h	Enthalpy	h_c	Heat transfer coefficient
κ	Thermal conductivity	V_{evap}	Evaporation recession speed
F	Volume fraction of fluid		

2. Materials and methods

2.1. Material and autogenous welding

The chemical composition of the studied AISI 316L stainless steel is reported as follows: 0.019C-0.514Si-1.32Mn-16.51Cr-10.46Ni-2.14Mo-0.401Cu-0.019Ti-0.089V-0.025P-0.008S-68.50Fe (in wt. %) according to ASTM A276. Autogenous welding was performed on a hot-rolled plate with a thickness of 12 mm, utilizing two advanced additive manufacturing machines: (i) the IRB 4600 DED machine equipped with a fiber laser of 500 μm spot size, operated at 1000 W and 11 mm/s, and (ii) the Mlab cusing R SLM system equipped with a fiber laser of 40 μm spot size, operated at a power of 95 W with various scan speeds ranging from 200 to 700 mm/s. Optical microscopy was employed to analyze the melt pool geometry and weld metal microstructure, with mechanically polished samples that were electrolytically etched in a solution containing 10 vol % oxalic acid at a voltage of 6 V.

2.2. Mechanistic modeling

Three-dimensional (3D) simulations of the temperature field and fluid flow were carried out for autogenous welding using both the DED and SLM machines. The simulations assumed a Newtonian and incompressible fluid under laminar flow conditions. The Finite Difference Method (FDM) was employed to solve the equations of mass conservation, momentum conservation, and energy conservation, as presented in equation (1) through (3), respectively. The solidus isotherm at 1650 K was used to trace the computational fusion boundary. The Volume of Fluid (VOF) technique, as described in equation (4) [48,49], was utilized to determine the surface of the melt pool. Table 1 provides a list of the modeling variables.

$$\nabla . \vec{v} = 0 \tag{1}$$

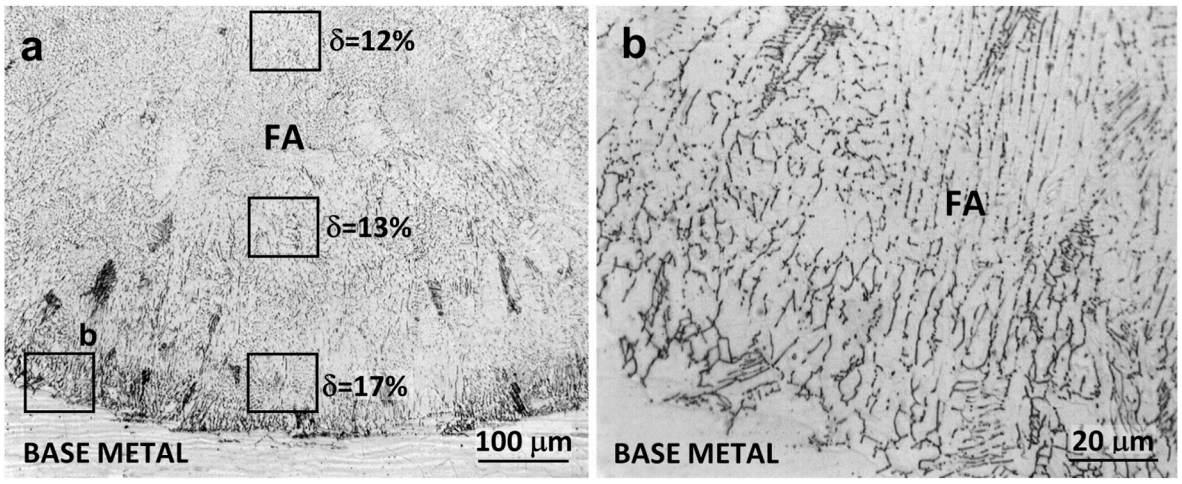

Fig. 1. Optical micrographs depicting the transverse section of the autogenous DED weld. Higher magnification in (b) provides a close view near the fusion boundary, revealing vermicular and lacy ferrite that signifies the prevalence of the FA mode.

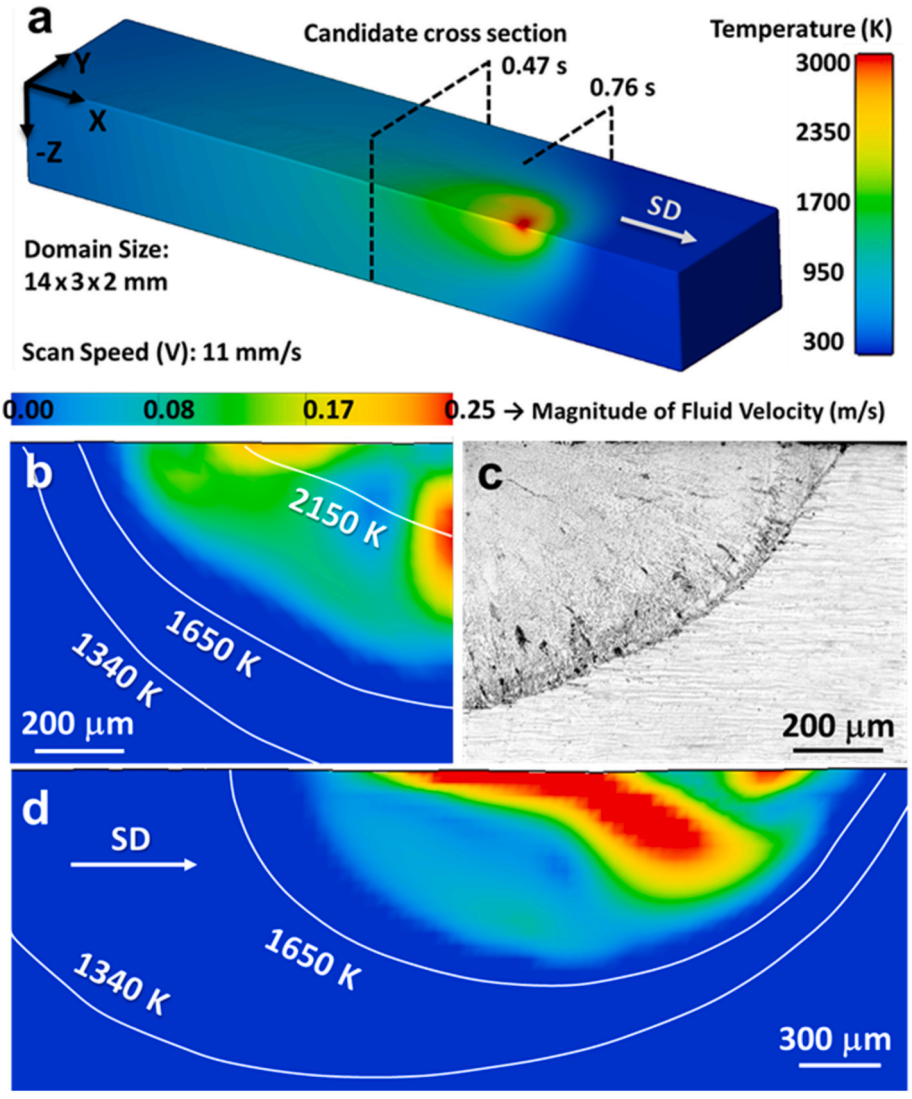

Fig. 2. Computational assessment of DED weld: (a) a perspective of the simulated temperature field, with the laser beam scan direction indicated as SD. The beam turns off at 0.76 ms; (b) a transverse view of the computed velocity field, along with temperature contours. This corresponds to a candidate cross section at 0.47 ms. The fusion boundary, outlined by the solidus contour at 1650 K, is compared with experimental counterpart in (c); (d) a longitudinal view of the velocity field and temperature contours.

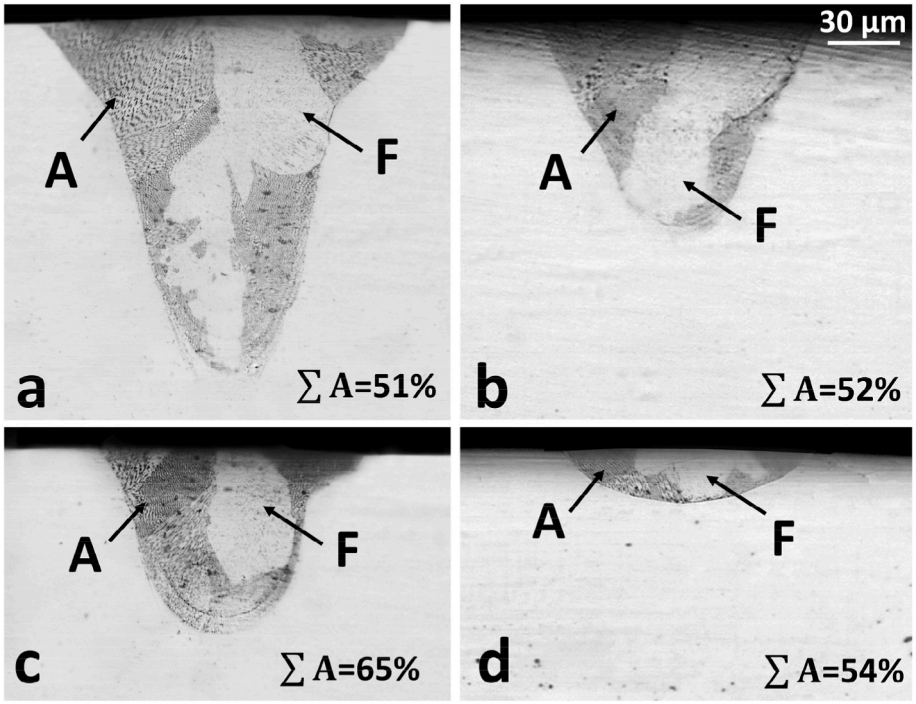

Fig. 3. Optical micrographs showing of the transverse section of the autogenous SLM welds conducted at different scan speeds (V): (a) V = 300 mm/s; (b) V = 500 mm/s; (c) V = 600 mm/s; (d) V = 700 mm/s. The term ∑A represents the total area percentage of the dark regions solidified with the A mode.

$$\frac{\partial \vec{v}}{\partial t} + (\vec{v}.\nabla)\vec{v} = -\frac{1}{\rho}\nabla p + \frac{\mu}{\rho}\nabla^2 \vec{v} - K\vec{v} + f \tag{2}$$

$$\frac{\partial h}{\partial t} + \vec{v}.\nabla h = \frac{1}{\rho}\nabla.\,(\kappa \nabla T) \tag{3}$$

$$\frac{\partial F}{\partial t} + (\vec{v}.\nabla)F = 0 \tag{4}$$

A laser beam was considered as a heat source which moves in the scan direction (SD), with a Gaussian distribution function as given in equation (5) [50,51]:

$$q = \frac{2\eta P}{\pi r^2}\exp\left(\frac{-2(x^2+y^2)}{r^2}\right) \tag{5}$$

The fluid flow pattern was assumed to be governed by the buoyancy force, surface tension, and recoil pressure, as written in equation (6) through (8), respectively [52].

$$F_b = -\rho g \beta (T - T_l) \tag{6}$$

$$\gamma = \gamma_0 + \frac{d\gamma}{dT}(T - T_0) \tag{7}$$

$$P_r = AB_0 T_s^{\frac{1}{2}} \exp\left(-\frac{U}{T_s}\right) \tag{8}$$

where A = 0.55 under atmospheric pressure and $B_0 = 1.78 \times 10^{10}$. The computational domain was discretized using rectangular cuboid cells of 50 µm for the DED model and 5 µm for the SLM. In both welding types, the initial temperature was set to the ambient temperature. As for the boundary conditions, the surface heat input Q was assumed according to equation (9):

$$K\frac{\partial T}{\partial \vec{n}} = Q - Q_{rad} - Q_{conv} - Q_{evap} \tag{9}$$

in which, heat losses due to radiation (Q_{rad}), convection (Q_{conv}), and evaporation (Q_{evap}) were calculated according to equation (10) through (12) [52]:

$$Q_{rad} = \sigma\varepsilon\left(T^4 - T_0^4\right) \tag{10}$$

$$Q_{conv} = h_c(T - T_0) \tag{11}$$

$$Q_{evap} = \rho V_{evap} T \tag{12}$$

In the conduction mode (DED), the impact of recoil pressure was neglected due to the maximum temperature being lower than the evaporation temperature, as explained in Ref. [53]. Additionally, it was assumed that multiple reflections in the keyhole are compensated for by increasing the nominal power. The thermophysical properties of 316L steel were adopted from Ref. [43].

2.3. Artificial neural networks modeling

The ORFN artificial neural networks model was employed to compute the ferrite volume percentage at various cooling rates [32]. This model comprises 14 nodes (13 elements plus the logarithm of the cooling rate) in the input layer, 6 nodes in the hidden layer, and 1 node in the output layer, which provides the ferrite number. Reference [32] provides the normalization parameters for the input data, weight parameters from the input layer to the hidden layer, as well as from the hidden layer to the output layer, and the de-normalization of the output data. The calculations were executed in an Excel spreadsheet following the formulation outlined in reference [20].

3. Results

Fig. 1 depicts optical micrographs of the autogenous DED weld. The austenite is represented by the light gray matrix, while the dark gray phase corresponds to residual ferrite. The volume percentage of residual ferrite was measured at about 17, 13 and 12 at the specified regions in Fig. 1a, which decreases with an increase in the distance from the melt pool bottom toward the center. There is also a gradual change in the morphology of residual ferrite, from vermicular/lacy into spherical,

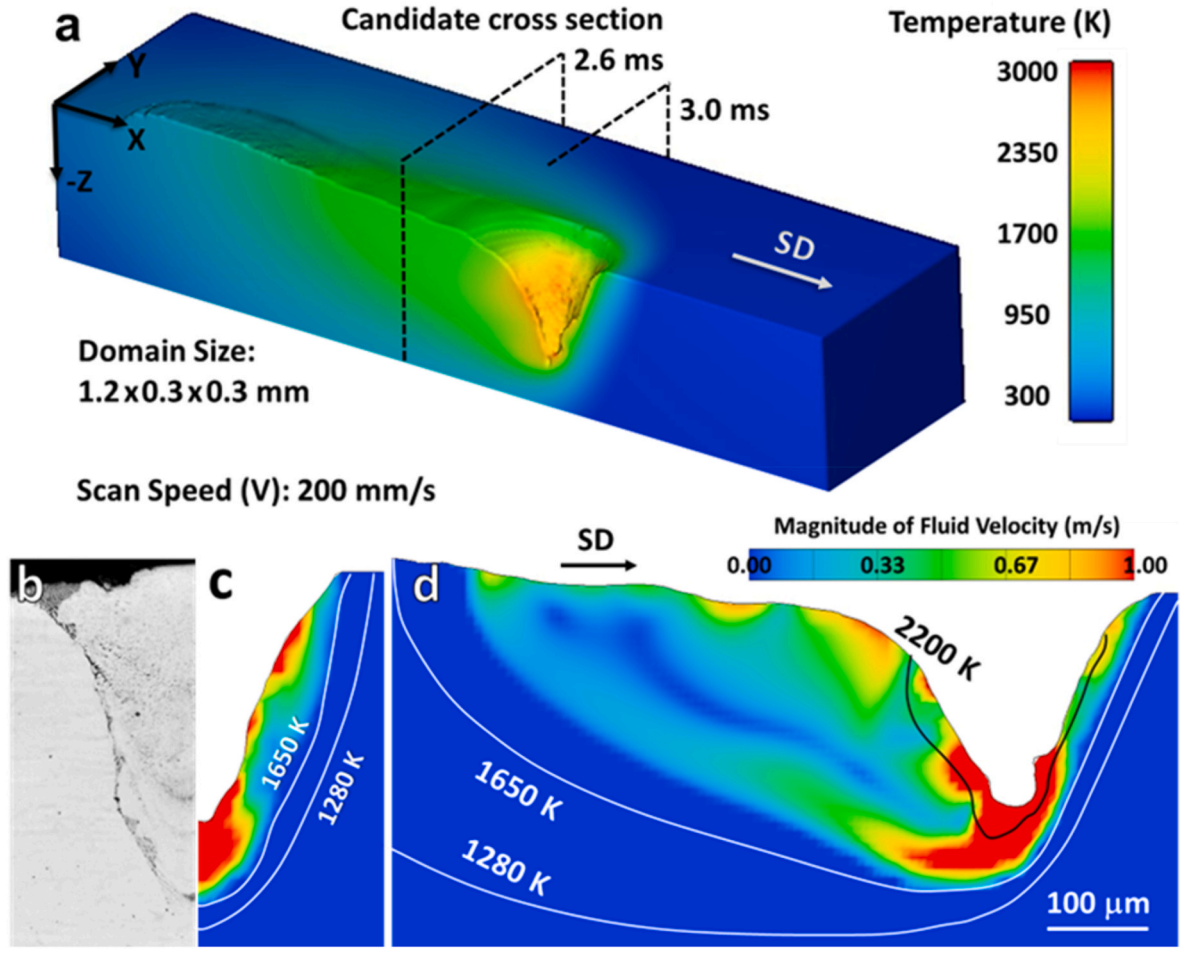

Fig. 4. Computational assessment of SLM weld: (a) a perspective of the computed temperature field, with the laser beam scanning at a velocity of 200 mm/s in the SD direction. The beam turns off at 3.0 ms; (b) optical micrograph depicting the experimental fusion boundary of the same condition; (c) a transverse view of the computed velocity field, along with temperature contours. This corresponds to a candidate cross section at 2.6 ms. Additionally, the fusion boundary, outlined by the solidus contour at 1650 K, is reasonably compared with its experimental counterpart in (b); (d) a longitudinal view of the velocity field and temperature contours.

with increasing the distance from the fusion boundary. The distinct vermicular and lacy morphologies of the residual ferrite near the fusion boundary suggest solidification through the FA mode (Fig. 1b). No alteration of the FA mode was observed in the interior region.

Fig. 2a provides a perspective of the simulated temperature field for DED weld. Meanwhile, Fig. 2b displays a transverse view of the computed velocity field, with superimposed temperature contours. Notably, the solidus contour at 1650 K represents the fusion boundary, which closely aligns with the experimental fusion boundary depicted in Fig. 2c. Additionally, Fig. 2d presents a longitudinal view of the computed velocity field and the temperature contours. In this view, one observes melting in the conduction mode, significant convection in the

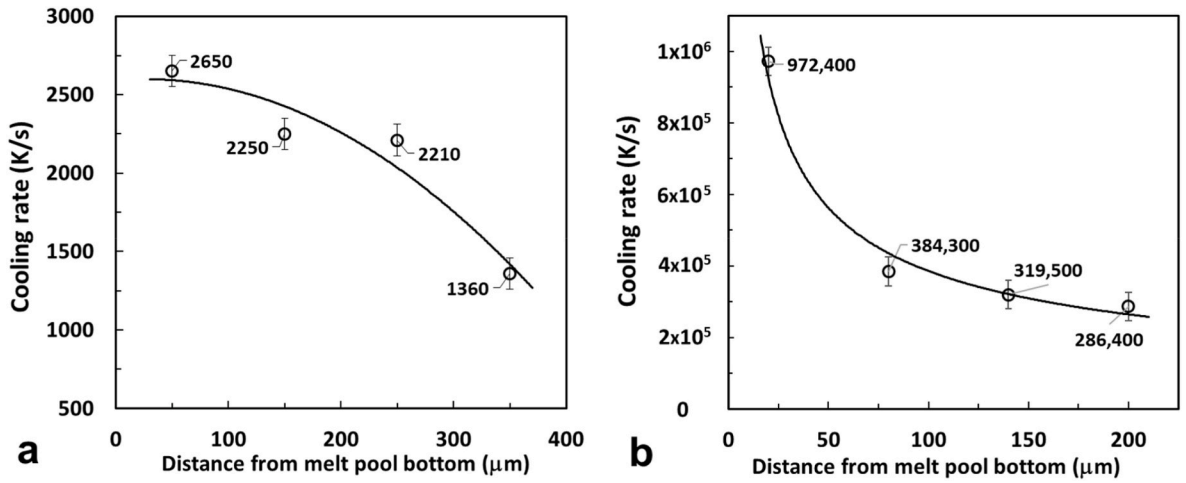

Fig. 5. Changes in the computed cooling rate with increasing the distance from the melt pool bottom; (a) DED weld; (b) SLM weld.

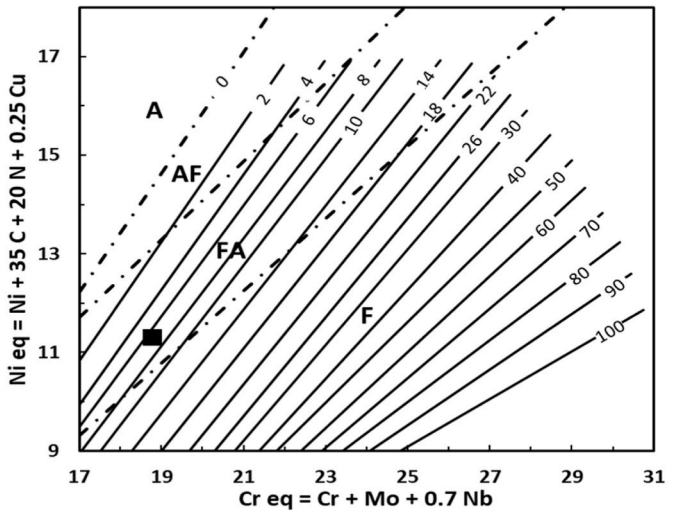

Fig. 6. Representation of the position of the examined 316L steel (represented by the solid square) on the WRC-1992 constitution diagram, reproduced with permission from the American Welding Society [16].

central zone, and minimal convection near the fusion boundary.

Fig. 3 displays optical micrographs of the transverse sections of autogenous SLM welds, conducted at a constant power of 95 W and scan speeds ranging from 300 to 700 mm/s. Considerable changes in melting mode and weld pool dimensions are observed with varying scan speeds. At low scan speeds, the keyhole mode is evident, altering to a shallow conduction mode at the highest speed. Within the optical micrographs, distinct darkly-etched and brightly-etched regions are discernible. Similar microstructures were studied by Godfrey et al. [40] in AISI 316L steel blocks printed using the SLM process. Their research suggested that the dark regions, termed fish-scale, result from solidification via the single-phase austenite (A) mode. In contrast, the bright regions result from solidification through the single-phase ferrite (F) mode, followed by the transformation of ferrite to massive austenite in the solid state. Regardless of the image contrast, the microstructure was consistently austenitic with residual ferrite accounting for less than 0.5 vol %. However, it exhibited distinct characteristic microsegregation patterns associated with the A and F modes. Consequently, solidification was presumed to commence with the A mode at the fusion boundary, altering to the F mode in the interior. This dual mode is identified at all scan speeds, but the total area fraction of dark regions ($\sum$A), solidified with the A mode, increases with higher scan speeds, except for the highest scan speed, where the melting mode shifted to a very shallow conduction mode.

A perspective of the simulated temperature field, Fig. 4a, features the keyhole mode melting for an SLM weld, conducted at a scan speed of 200 mm/s. Fig. 4b and c offer a comparison between the experimental and the simulated fusion boundaries. The solidus contour at 1650 K confirms that the simulated fusion boundary closely aligns with the experimental fusion boundary. Fig. 4d presents the corresponding longitudinal section of the computed velocity field and temperature contours. Considerable convection is identified in the bulk liquid, while there is negligible convection near the trailing fusion boundary.

An average cooling rate between 1700 K and 1650 K was calculated as a measure of cooling rate during solidification. Fig. 5 shows changes in the cooling rates for simulated DED and SLM welds. The cooling rate decreases with increasing the distance from the melt pool bottom in both DED and SLM welds. However, for a given distance from the melt pool bottom, the SLM weld shows substantially higher cooling rate, at least two orders of magnitude, than the DED weld. An average value of 2118 K/s and 490650 K/s is determined for the DED and SLM welds, respectively.

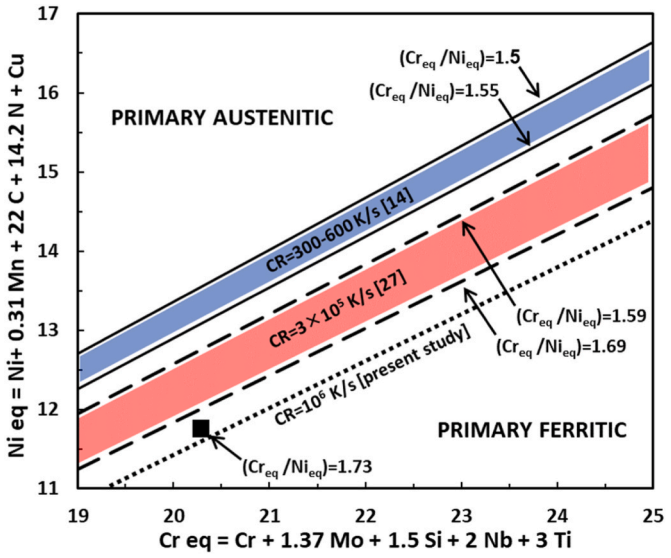

Fig. 7. A constitution diagram illustrating the modification range of solidification mode as a function of cooling rate (CR), based on the Hammar-Svensson equivalents. The solid square denotes the position of the studied 316L steel at Cr_{eq} = 20.3, Ni_{eq} = 11.7, Cr_{eq}/Ni_{eq} = 1.73. This diagram is used with permission from Springer and Taylor & Francis [13,30].

4. Discussion

The elevated cooling rate significantly impacted the solidification behavior of the present steel. In the DED weld, the primary solidification mode (FA) persisted throughout the entire solidification stage. However, variations in the cooling rate, correlated with increasing distance from the melt pool bottom, resulted in a noteworthy variation in residual ferrite content. The effects of the cooling rate were particularly pronounced in the SLM welds, leading to a transition into the distinct A and F regions. In both cases, the resulting microstructural consequences could potentially influence the physical and mechanical properties of the weld metals. Therefore, the discussion now delves into the assessment of available tools for predicting cooling rate-dependent microstructural evolution.

In Fig. 6, the position of the present steel (represented by the solid square) is illustrated on the WRC-1992 constitution diagram, the latest diagram proposed for predicting conventional weld metal microstructures [16]. According to this prediction, the steel is expected to solidify with the FA mode, yielding approximately 6–8 vol % of residual ferrite at room temperature. While the predicted FA mode aligns with the DED weld, the estimated amount of residual ferrite is underestimated when compared to Fig. 1. The acceleration of the cooling rate hinders the diffusional transformation of primary ferrite to austenite in the solid state, leading to an increased amount of residual ferrite at ambient temperature [32,40]. The observation of the dual mode (A + F) in the SLM welds significantly deviates from the WRC-1992 prediction.

Fig. 7 illustrates a constitution diagram accounting for a modification range of solidification mode at high cooling rates, based on the Hammar-Svensson equivalents. As a predictive tool, this diagram delineates the solidification mode as a function of the Cr_{eq}/Ni_{eq} ratio and cooling rate. According to Suutala et al. [13], alloys with Cr_{eq}/Ni_{eq} ratios ranging from 1.50 to 1.55 are prone to a modification of solidification mode during gas tungsten arc (GTA) welding, transitioning from primary ferritic to primary austenitic within this range. Above and below the modification range, the solidification modes are primarily austenitic and primarily ferritic, respectively. Lienert and Lippold [30] reported that, during pulsed laser welding, alloys within the composition range of Cr_{eq}/Ni_{eq} = 1.59 to Cr_{eq}/Ni_{eq} = 1.69 undergo modification of solidification mode, exhibiting a dual solidification mode (the distinct regions

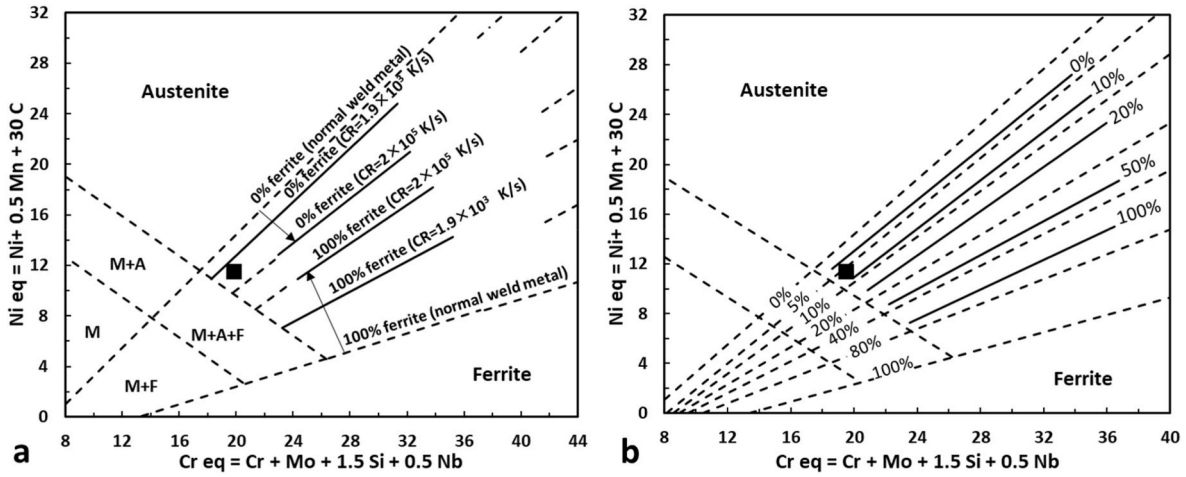

Fig. 8. The position of the studied alloy: (a) on the implicated Schaeffler diagram illustrating the effect of cooling rate (CR), used with permission from Taylor & Francis [31]; (b) on the implicated Schaeffler diagram calculated for a cooling rate of 1.9×10^3 K/s as comparable to the DED weld, used with permission from the Japan Welding Society [23].

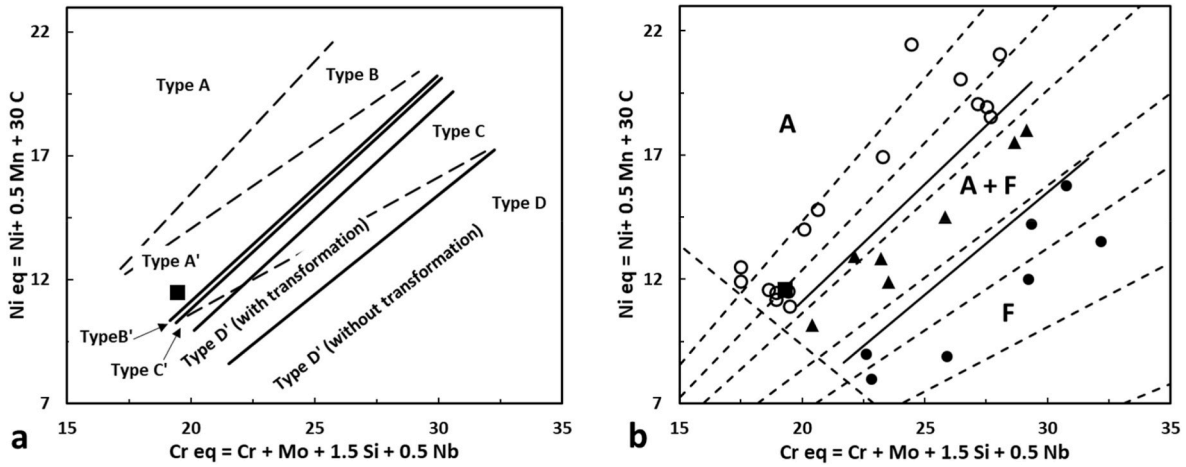

Fig. 9. Demonstrating the position of the present steel (solid square) on implicated diagrams based on the Schaeffler equivalents. These diagrams are proposed for pulsed laser welds cooled at a rate of 2×10^5 K/s. (a) Predicting solidification with type A′ (the A mode) for the present SLM weld; (b) predicting a fully austenitic microstructure for the present SLM weld. In these diagrams, open circles, triangles, and solid circles indicate fully austenitic, duplex, and fully ferritic microstructures, respectively. This figure is used with permission from the Laser Institute of America [26].

solidified with A and F modes within the same weld metal). The estimated cooling rate during GTA welding ranged from 300 to 600 K/s, while pulsed laser welds were estimated to cool at a rate of 3 × 105 K/s, based on dendritic arms spacing measurements. Considering the position of the present steel in Fig. 7 (indicated by the solid square) and the computed cooling rates, one would anticipate the FA mode for the DED weld, aligning with the experimental observation. The identification of the dual mode in the SLM welds is not far from expectations, especially when considering the higher cooling rate determined here. Therefore, this diagram reasonably predicts the solidification mode of the DED weld and signals a potential modification in the SLM welds.

According to Nishimoto [31], a high cooling rate affects the Schaeffler diagram, causing a displacement of ferrite lines that contracts the duplex austenite-ferrite region, as illustrated in Fig. 8a. In alloys solidifying with the AF mode, residual ferrite diminishes with an increasing cooling rate, while in alloys solidifying with the FA mode, it increases. Based on the position of the present steel, a duplex austenite-ferrite microstructure is anticipated at cooling rates around 1.9×10^3 K/s, which aligns with the cooling rate computed for the DED weld. Conversely, it is expected to yield single-phase austenite at cooling rates exceeding 2×10^5 K/s, comparable to the cooling rate computed for the present SLM weld. Nakao et al. [23] reported implicated Schaeffler diagrams for various cooling rates. Fig. 8b locates the studied 316L steel on the implicated Schaeffler diagram proposed for a cooling rate of 1.9×10^3 K/s [23]. The microstructure of the present steel at this cooling rate is predicted to consist of austenite and less than 10 vol % residual ferrite, still underestimated compared to the DED weld.

Katayama et al. [26] and David et al. [27] presented implicated Schaeffler diagrams for stainless steel laser welds solidifying at extremely high cooling rates. Fig. 9 displays implicated diagrams calculated for pulsed laser welds of stainless steels at a cooling rate of 2×10^5 K/s. The regions solidified with A, AF, FA, and F modes during conventional welding are denoted as types A, B, C, and D, respectively. Correspondingly, these regions have been changed to the primed counterparts (A′, B′, C′, and D′) at an extremely high cooling rate.

Based on the position of the present steel on these diagrams (see the solid squares), solidification with type A′ is anticipated, resulting in a fully austenitic microstructure as predicted for the present SLM welds. Similar predictions were obtained using diagrams reported in Ref. [39]. It is noted that solidification consistently initiates with the A mode at the fusion boundary, but the subsequent alteration to the F mode is not specified. Godfrey et al. [40], based on the computation of solidification

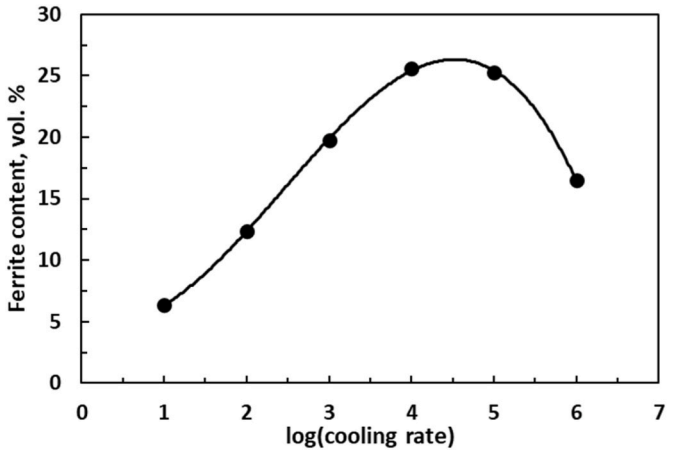

Fig. 10. Expected variation of ferrite content with the cooling rate (K/s) in the present steel as calculated using the ORFN model. Courtesy of J.M. Vitek and co-authors [33].

parameters and the variation of the interface response function with solidification rate, demonstrated that the A mode, initiated at the fusion boundary, is replaced by the F mode at a critical solidification rate due to spatial and temporal variations in solidification parameters, e.g., the temperature gradient in the melt (G) and the solidification rate (R). Therefore, further advancement in the field is required to predict the dual mode by accounting for temporal variations in the melt pool.

Fig. 10 illustrates the expected variation in residual ferrite content with cooling rate, as calculated using the ORFN model. This model predicts increasing ferrite content for the present alloy composition with increasing cooling rate to 30000 K/s, after which further escalation in the cooling rate may lead to a decline in the ferrite content, in line with the predominance of the FA and AF modes, respectively. With cooling rate variation in the range of 1360–2650 K/s, calculated for the present DED weld, the ferrite content is anticipated to change for a few percent. This prediction aligns qualitatively with the observed variation in ferrite content within the DED weld metal.

5. Conclusion

Autogenous welds performed by powderless DED and SLM machines demonstrated a broad range of cooling rates, based on the mechanistic modeling aiming at accurate numerical computations of temperature field and cooling rate. The investigation of the solidification microstructure in AISI 316L steel indicated alterations in the solidification mode at exceptionally high cooling rates within the SLM welds. The assessment of the predictive capacity of available tools for solidification microstructure was conducted as follows.

1) A constitution diagram, employing the Hammar-Svensson equivalents, predicted modifications in the solidification mode based on the Cr_{eq}/Ni_{eq} ratio and cooling rate.
2) Predictions from WRC-1992 and a Schaeffler diagram, developed for a comparable cooling rate, aligned with the identification of the FA mode in the DED weld.
3) The initial A mode observed at the fusion boundary of SLM welds consistently matched predictions by the Schaeffler diagram designed for extremely high cooling rates. However, subsequent transformation to the F mode was not accounted for.
4) The ORFN model qualitatively anticipated an increase in ferrite content with a rising cooling rate toward the melt pool bottom.

Declaration of competing interest

The authors declare that they have no known competing financial interests or personal relationships that could have appeared to influence the work reported in this paper.

References

[1] Davis J. ASM specialty handbook: stainless steels. ASM international; 1994.
[2] Adeyemi A, Akinlabi E, Mahamood R. Powder bed based laser additive manufacturing process of stainless steel: a review. Mater Today Proc 2018;5:18510–7. https://doi.org/10.1016/j.matpr.2018.06.193.
[3] Bajaj P, Hariharan A, Kini A, Kürnsteiner P, Raabe D, Jägle EA. Steels in additive manufacturing: a review of their microstructure and properties. Mater. Sci. Eng. A. 2020;772:138633. https://doi.org/10.1016/j.msea.2019.138633.
[4] Haghdadi N, Laleh M, Moyle M, Primig S. Additive manufacturing of steels: a review of achievements and challenges. J Mater Sci 2021;56:64–107. https://doi.org/10.1007/s10853-020-05109-0.
[5] Jin W, Zhang C, Jin S, Tian Y, Wellmann D, Liu W. Wire Arc additive manufacturing of stainless steels: a review. Appl Sci 2020;10. https://doi.org/10.3390/app10051563.
[6] Krakhmalev P, Fredriksson G, Svensson K, Yadroitsev I, Yadroitsava I, Thuvander M, Peng R. Microstructure, solidification texture, and thermal stability of 316 L stainless steel manufactured by laser powder bed fusion. Metals 2018;8. https://doi.org/10.3390/met8080643.
[7] Michla JRJ, Nagarajan R, Krishnasamy S, Siengchin S, Ismail SO, Prabhu TR. Conventional and additively manufactured stainless steels: a review. Trans Indian Inst Met 2021;74:1261–78. https://doi.org/10.1007/s12666-021-02305-7.
[8] Siefert JA, David SA. Weldability and weld performance of candidate austenitic alloys for advanced ultrasupercritical fossil power plants. Sci Technol Weld Join 2014;19:271–94. https://doi.org/10.1179/1362171814Y.0000000197.
[9] Brooks JA, Thompson AW. Microstructural development and solidification cracking susceptibility of austenitic stainless steel welds. Int Mater Rev 1991;36:16–44. https://doi.org/10.1179/imr.1991.36.1.16.
[10] Lo KH, Shek CH, Lai JKL. Recent developments in stainless steels. Mater Sci Eng R Rep 2009;65:39–104. https://doi.org/10.1016/j.mser.2009.03.001.
[11] Kou S. Welding metallurgy. third ed. WILEY; 2020.
[12] Lippold JC, Kotecki DJ. Welding metallurgy and weldability of stainless steels. 2005.
[13] Suutala N. Effect of solidification conditions on the solidification mode in austenitic stainless steels. Metall Trans A 1983;14:191–7. https://doi.org/10.1007/BF02651615.
[14] Schaeffler AL. Constitution diagram for stainless steel weld metal. Met. Prog. 1949;56:680.
[15] Delong WT. Ferrite in austenitic stainless steel weld metal. Weld Res 1974;53:273s–86s.
[16] Kotecki DJ, Siewart TA. WRC-1992 constitution diagram for stainless steel weld metals: a modification of the WRC-1988 diagram. Weld. J.; 1992. p. 171s–8s.
[17] Olson DL. Prediction of austenitic weld metal microstructure and properties. Weld J 1985;64:281s–95s.
[18] Bermejo MAV. Predictive and measurement methods for delta ferrite determination in stainless steels. Weld J 2012;91:113–1212.
[19] Vitek JM, Iskander YS, Oblow EM. Improved ferrite number prediction in stainless steel arc welds using artificial neural networks - Part 1: neural network development. Weld J 2000;79. 33-s.
[20] Vitek JM, Iskander YS, Oblow EM. Improved ferrite number prediction in stainless steel arc welds using artificial neural networks - Part 2: neural network results. Weld J 2000;79:41–s.
[21] Vasudevan M, Bhaduri AK, Raj B. Prediction of ferrite number in stainless steel welds using Bayesian Neural Network model. Weld World 2007;51:15–28. https://doi.org/10.1007/BF03266582.
[22] Elmer JW, Allen SM, Eagar TW. Microstructural development during solidification of stainless steel alloys. Metall Trans A 1989;20:2117–31.
[23] Nakao Y, Nishimoto K, Zhang WP. Effects of rapid solidification by laser surface melting on solidification modes. Study on laser surface modification of stainless steels. Q J Jpn Weld Soc 1989;7:130–7.
[24] Vitek JM, Dasgupta A, David SA. Microstructural modification of austenitic stainless steels by rapid solidification. Metall Trans A 1983;14:1833–41.
[25] Brooks JA, Williams JC, Thompson AW. Microstructural origin of the skeletal ferrite morphology of austenitic stainless steel welds. Metall Trans A 1983;14:1271–81.
[26] Katayama S, Matsunawa A. Solidification microstructure of laser welded stainless steels. Int. Congr. Appl. Lasers Electro-Optics 1984:60–7. https://doi.org/10.2351/1.5057623.
[27] David SA, Vitek JM, Reed RW, Hebble TL. Effect of rapid solidification on stainless steel weld metal microstructures and its implications on the Schaeffler diagram. Weld J. 1987;66. 289-s.
[28] Fukumoto S, Kurz W. Prediction of the δ to γ transition in austenitic stainless steels during laser treatment. ISIJ Int 1998;38:71–7. https://doi.org/10.2355/isijinternational.38.71.
[29] Lippold JC. Solidification behavior and cracking susceptibility of pulsed-laser welds in austenitic stainless steels. Weld J Incl Weld Res Suppl 1994;73:129s.
[30] Lienert TJ, Lippold JC. Improved weldability diagram for pulsed laser welded austenitic stainless steels. Sci Technol Weld Join 2003;8:1–9. https://doi.org/10.1179/136217103225008847.
[31] Nishimoto K. Prediction of weld metal microstructure: stainless steels. Weld Int 1992;6:848–52. https://doi.org/10.1080/09507119209548301.

[32] Vitek JM, David S, Hinman CR. Improved ferrite number prediction model that accounts for cooling rate effects - Part 1: model development. Weld J 2003;82. 10-s.
[33] Vitek JM, David SA, Hinman CR. Improved ferrite number prediction model that accounts for cooling rate effects - Part 2: model results. Weld J 2003;82. 43-s.
[34] Kianersi D, Mostafaei A, Amadeh AA. Resistance spot welding joints of AISI 316L austenitic stainless steel sheets: phase transformations, mechanical properties and microstructure characterizations. Mater Des 2014;61:251–63. https://doi.org/10.1016/j.matdes.2014.04.075.
[35] Guo P, Zou B, Huang C, Gao H. Study on microstructure, mechanical properties and machinability of efficiently additive manufactured AISI 316L stainless steel by high-power direct laser deposition. J Mater Process Technol 2017;240:12–22. https://doi.org/10.1016/j.jmatprotec.2016.09.005.
[36] Mukherjee M. Effect of build geometry and orientation on microstructure and properties of additively manufactured 316L stainless steel by laser metal deposition. Materialia 2019;7:100359. https://doi.org/10.1016/j.mtla.2019.100359.
[37] Saboori A, Aversa A, Bosio F, Bassini E, Librera E, De Chirico M, Biamino S, Ugues D, Fino P, Lombardi M. An investigation on the effect of powder recycling on the microstructure and mechanical properties of AISI 316L produced by Directed Energy Deposition. Mater. Sci. Eng. A. 2019;766:138360. https://doi.org/10.1016/j.msea.2019.138360.
[38] Tan ZE, Pang JHL, Kaminski J, Pepin H. Characterisation of porosity, density, and microstructure of directed energy deposited stainless steel AISI 316L. Addit Manuf 2019;25:286–96. https://doi.org/10.1016/j.addma.2018.11.014.
[39] Hossein Nedjad S, Yildiz M, Saboori A. Solidification behaviour of austenitic stainless steels during welding and directed energy deposition. Sci Technol Weld Join 2023;28:1–17. https://doi.org/10.1080/13621718.2022.2115664.
[40] Godfrey AJ, Simpson J, Leonard D, Sisco K, Dehoff RR, Babu SS. Heterogeneity and solidification pathways in additively manufactured 316L stainless steels. Metall Mater Trans A 2022;53:3321–40. https://doi.org/10.1007/s11661-022-06747-6.
[41] Du Y, Mukherjee T, DebRoy T. Physics-informed machine learning and mechanistic modeling of additive manufacturing to reduce defects. Appl Mater Today 2021;24:101123. https://doi.org/10.1016/j.apmt.2021.101123.
[42] DebRoy T, Mukherjee T, Wei HL, Elmer JW, Milewski JO. Metallurgy, mechanistic models and machine learning in metal printing. Nat Rev Mater 2021;6:48–68. https://doi.org/10.1038/s41578-020-00236-1.
[43] Wei HL, Mukherjee T, Zhang W, Zuback JS, Knapp GL, De A, DebRoy T. Mechanistic models for additive manufacturing of metallic components. Prog Mater Sci 2021;116:100703. https://doi.org/10.1016/j.pmatsci.2020.100703.
[44] Wei HL, Bhadeshia HKDH, David SA, Debroy T, Bhadeshia HKDH, David SA, Debroy T. Harnessing the scientific synergy of welding and additive manufacturing. Sci Technol Weld Join 2019;24:1–6. https://doi.org/10.1080/13621718.2019.1615189.
[45] Saboori A, Aversa A, Marchese G, Biamino S, Lombardi M, Fino P. Microstructure and mechanical properties of AISI 316L produced by directed energy deposition-based additive manufacturing: a review. Appl Sci 2020;10. https://doi.org/10.3390/app10093310.
[46] Röttger A, Boes J, Theisen W, Thiele M, Esen C, Edelmann A, Hellmann R. Microstructure and mechanical properties of 316L austenitic stainless steel processed by different SLM devices. Int J Adv Manuf Technol 2020;108:769–83. https://doi.org/10.1007/s00170-020-05371-1.
[47] Großwendt F, Becker L, Röttger A, Chehreh AB, Strauch AL, Uhlenwinkel V, Lentz J, Walther F, Fechte-Heinen R, Weber S, Theisen W. Impact of the allowed compositional range of additively manufactured 316L stainless steel on processability and material properties. Materials 2021;14. https://doi.org/10.3390/ma14154074.
[48] Lee Jae Y, Ko Sung H, Farson Dave F, Yoo Choong D. Mechanism of keyhole formation and stability in stationary laser welding. J Phys D Appl Phys 2002;35:1570. https://doi.org/10.1088/0022-3727/35/13/320.
[49] Hamed Zargari H, Ito K, Sharma A. Effect of workpiece vibration frequency on heat distribution and material flow in the molten pool in tandem-pulsed gas metal arc welding. Int J Adv Manuf Technol 2023;129:2507–22. https://doi.org/10.1007/s00170-023-12424-8.
[50] Promoppatum P, Yao S-C, Pistorius PC, Rollett AD. A comprehensive comparison of the analytical and numerical prediction of the thermal history and solidification microstructure of inconel 718 products made by laser powder-bed fusion. Engineering 2017;3:685–94. https://doi.org/10.1016/J.ENG.2017.05.023.
[51] Wu Y, San C, Chang C, Lin H-J, Marwan R, Baba S, Hwang W-S. Numerical modeling of melt-pool behavior in selective laser melting with random powder distribution and experimental validation. J Mater Process Technol 2018;254:72–8. https://doi.org/10.1016/j.jmatprotec.2017.11.032.
[52] Wu D, Hua X, Huang L, Zhao J. Numerical simulation of spatter formation during fiber laser welding of 5083 aluminum alloy at full penetration condition. Opt Laser Technol 2018;100:157–64. https://doi.org/10.1016/j.optlastec.2017.10.010.
[53] Kan X, Yin Y, Yang D, Li W, Sun J. Micro pool characteristics of 316L and the influence of sulfur during SLM. Opt Laser Technol 2021;142:107136. https://doi.org/10.1016/j.optlastec.2021.107136.